

Original article

Non-monotonic effect of permeability and wettability on immiscible displacement dynamics in porous media

Wenbo Gong¹, Yaru Liu², Cheng Dai³, Jiangtao Zheng², Zhiqiang Chen³, Wei Zhao⁴, Junchao Li⁵*

Keywords:

Wettability effect permeability variation immiscible displacement three-dimensional porous media lattice Boltzmann method

Cited as:

Gong, W., Liu, Y., Dai, C., Zheng, J., Chen, Z., Zhao, W., Li, J. Non-monotonic effect of permeability and wettability on immiscible displacement dynamics in porous media. Capillarity, 2025, 17(2): 54.67

https://doi.org/10.46690/capi.2025.11.02

Abstract:

The immiscible displacement behavior in porous media is crucial for oil recovery and subsurface remediation, yet how wettability influences this process across different pore structures remains unclear. Using a color-gradient lattice Boltzmann model, this study investigates immiscible displacement dynamics in porous media. Heterogeneous porous structures with various degrees of permeability were reconstructed using the quarter structure generation set algorithm, and wettability effects were analyzed with the contact angle set in the range of 30° to 150°. The numerical results showed that porous heterogeneity greatly affects the displacement efficiency via permeability-dependent flow pathway optimization. Enhanced efficiency was observed in high-permeability media through low-tortuosity channels, whereas low-permeability systems exhibited reduced efficiency due to capillary trapping in pores with lower flow capacity. Wettability alters displacement patterns via capillary forces - under hydrophilic condition, the displacing fluid preferentially enters smaller pores. Fractal dimension and Euler number were used to quantify flow heterogeneity, revealing that increased permeability reduces flow complexity and improves connectivity. Moreover, permeability heterogeneity and wettability interact to disrupt classical linear flow responses, leading to non-monotonic efficiency trends in lowpermeability systems. These findings highlight the importance of pore-scale multiphase flow in heterogeneous media and offer new insights for predicting wettability effects in subsurface flows.

1. Introduction

Studying immiscible two-phase flow in porous media holds fundamental importance across a wide range of scientific and engineering disciplines. For instance, from the perspectives of energy and environmental applications, it provides the mechanistic basis for carbon dioxide geological sequestration (Deng et al., 2017; Heinemann et al., 2021; Prasad et al., 2023; Massarweh and Abushaikha, 2024), remediation of groundwater contamination (Cai et al., 2024; Li et al., 2024; Yang et al., 2020, 2021, 2025), and enhanced oil recovery in petroleum reservoirs (Holtzman and Segre, 2015; Li et al., 2018; Hu et al., 2019; Jackson et al., 2020). Beyond these applications,

Yandy Scientific Press

*Corresponding author.

E-mail address: wenbog@cup.edu.cn (W. Gong); 15930101070@163.com (Y. Liu); daicheng.syky@sinopec.com (C. Dai); zhengjt@cumtb.edu.cn (J. Zheng); chenzhiqiang.syky@sinopec.com (Z. Chen); zhaowei@student.cup.edu.cn (W. Zhao). 2709-2119 © The Author(s) 2025.

Received August 11, 2025; revised September 6, 2025; accepted September 28, 2025; available online October 1, 2025.

¹College of Safety and Ocean Engineering, China University of Petroleum, Beijing 102249, P. R. China

²State Key Laboratory for Fine Exploration and Intelligent Development of Coal Resources, China University of Mining and Technology, Beijing 100083, P. R. China

³Petroleum Exploration and Production Research Institute, SINOPEC, Beijing 102206, P. R. China

⁴State Key Laboratory of Petroleum Resources and Engineering, China University of Petroleum, Beijing 102249, P. R. China

⁵Mechanical Engineering College, Xi'an Shiyou University, Xi'an 710065, P. R. China

insights into two-phase transport processes inspire bio-inspired designs such as water management in plant-based biomimetic materials (Wei et al., 2016; Wang, 2017; Zhan et al., 2018; Peng et al., 2022). The flow behavior of immiscible fluids is fundamentally governed by nonlinear multiphase dynamics, in which pore-scale heterogeneity, rock wettability, and intrinsic fluid properties collectively determine the displacement pathways and macroscopic transport efficiency.

Among the above factors, wettability plays a particularly prominent role. Defined as the preferential affinity of a solid surface toward a specific fluid phase, wettability controls pore invasion sequences, capillary entry pressures, and the spatial distribution of residual phases (Cieplak and Robbins, 1988; Holtzman and Segre, 2015). Classical pore-scale studies have consistently suggested that greater hydrophilicity stabilizes invasion fronts and enhances recovery efficiency (Cieplak and Robbins, 1988; Hu2019), forming the theoretical foundation of conventional displacement modeling and enhanced oil recovery design. However, recent experimental advances have challenged this monotonic paradigm. Microfluidic studies and pore-network experiments have reported non-monotonic behaviors, in which intermediate wettability conditions yield higher displacement efficiency compared with strongly waterwet or oil-wet states (Jung et al., 2016; Singh et al., 2017; Lei et al., 2022, 2023). These findings emphasize that cooperative pore-filling dynamics and capillary threshold balancing emerge in disordered structures, which are processes not accounted for in the classical wettability theory. Despite these insights, most studies continue to treat wettability as an isolated factor, without considering its interplay with structural heterogeneity.

Pore-scale heterogeneity is an equally influential factor, which encompasses variations in pore size distribution, connectivity and structural anisotropy. Extensive experimental and modeling studies have demonstrated that heterogeneity intensifies viscous fingering, fosters preferential flow channel formation, and modifies capillary trapping (Holtzman, 2016; Li et al., 2019; Wu et al., 2021). More recent efforts have attempted to integrate heterogeneity into coupled capillaryviscous competition frameworks (Holtzman and Segre, 2015; Jiang et al., 2013), highlighting the topological controls on displacement front evolution. Such frameworks often rely on simplified assumptions of static or homogeneous wettability, thereby neglecting the complex interactions between wettability gradients and structural heterogeneity. In fact, heterogeneity reshapes local capillary pressure distributions, alters entry thresholds, and interacts with wettability contrasts to produce bifurcating flow paths and cooperative pore-filling processes. As a result, although previous studies identified monotonic and non-monotonic wettability effects, the connection between these effects and pore structure permeability remains poorly understood, and the mechanisms driving the transition between monotonic and non-monotonic regimes have not been fully elucidated.

Experimental approaches aimed at resolving these coupled effects face notable limitations. High-resolution X-ray CT imaging allows the three-dimensional (3D) visualization of pore networks (Li et al., 2019), whereas its high cost and limited temporal resolution constrain its applicability to dynamic

studies, leading to static characterization being predominant. Microfluidic experiments, although valuable for visualizing displacement at the pore scale, are typically restricted to quasitwo-dimensional geometries, where preferential flow channels may be imposed by design, limiting the extrapolation of results to natural 3D porous systems. Furthermore, surface treatments employed to control wettability in microfluidic devices may not accurately reproduce the mineralogical and chemical properties of natural rock surfaces. These limitations hinder the systematic investigation of wettability-heterogeneity interactions under reservoir-relevant conditions.

Numerical modeling offers an effective alternative for probing the above mechanisms. Digital rock reconstruction methods, such as the quartet structure generation set (QSGS), attribute controllable heterogeneity and validated topological features to statistically representative porous media (Wang et al., 2007a, 2007b; Lei et al., 2020). While computational approaches, including pore-network models, finite volume methods, and phase-field formulations, have each advanced the understanding of multiphase flow, they involve tradeoffs between accuracy, computational cost and interface representation. The lattice Boltzmann method (LBM), rooted in kinetic theory, has emerged as a particularly promising approach. By modeling fluid evolution as particle distribution dynamics on discrete lattices, LBM naturally captures the interfacial processes without explicit interface tracking (Zhang and Wang, 2015; Ju et al., 2020; Zheng et al., 2021; Zhou et al., 2024). Its local and explicit computational structure affords excellent parallel scalability, rendering it well-suited for simulating multiphase displacement in complex porous geometries. In fact, LBM has been successfully applied in contexts such as petroleum recovery, CO2 sequestration, and underground hydrogen storage, demonstrating robustness in incorporating wettability effects, dynamic contact lines, and pore-scale heterogeneity (Ju et al., 2022; Bocanegra et al., 2024).

Building on these foundations, the present study aims to address the knowledge gap regarding the coupled influence of wettability and pore-scale heterogeneity on immiscible two-phase displacement. Using LBM-based digital core simulations, we demonstrate how the effect of wettability evolves from monotonic to non-monotonic regimes across porous structures with different permeability characteristics, and elucidate the mechanistic role of heterogeneity in driving this transition. By clarifying these mechanisms, this work enhances the theoretical and computational understanding of multiphase flow in complex geological formations, thereby providing valuable insights for reservoir management, CO₂ storage, as well as broader subsurface energy and environmental applications.

2. Lattice Boltzmann method

2.1 Governing equations

The LBM discretizes fluid motion into particle distribution functions that evolve through collision and streaming processes at the mesoscopic scale, inherently supporting efficient parallelization (Ju et al., 2020; Zheng et al., 2021). For multiphase flow, several LBM formulations exist, including the

color-gradient model (Huang et al., 2013), pseudo-potential model (Shan and Chen, 1993), free-energy model (Swift et al., 1995), and mean-field model. Among these, the colorgradient approach is employed in this study due to its strict phase-wise mass conservation, tunable surface tension, and superior numerical performance under large viscosity ratios (Huang et al., 2013). This method distinguishes immiscible fluids via separate distribution functions, while interfacial dynamics are captured through recoloring operations and specialized collision rules. Furthermore, the multiple-relaxationtime (MRT) scheme is incorporated to enhance numerical stability and accuracy in heterogeneous porous geometries (Leclaire et al., 2013, 2014; Leclaire et al., 2016). When applied simultaneously, these improvements provide a robust framework for investigating immiscible displacement in digital rock models under a wide range of reservoir conditions.

The density distribution function, as a fundamental variable in the lattice Boltzmann method, describes the distribution of particle densities at each discrete lattice point, migrating along specific discrete directions. This section focuses on two-phase fluid flow in 3D space. The D3Q19 model is used, which has 19 discrete velocities in 3D space (Chen et al., 2019). The total particle distribution function for the fluid mixture at position (x, t) is defined as follows:

$$f_i(x,t) = f_i^r(x,t) + f_i^b(x,t)$$
 (1)

The lattice Boltzmann equations for fluids r and b are given below:

$$f_i^{w}(x + e_i \delta t, t + \delta t) = f_i^{w}(x, t) + \Omega_i^{2, w} \{ \Omega_i^{1} + \bar{F}_i \},$$

$$w = r, b, i = 0, \dots, 18$$
(2)

where the superscript "w" stands for fluid r or b, and e_i represents the lattice velocities of the D3Q19 model. The unit speed components of the D3O19 model are represented as follows:

 $[e_0, e_1, e_2, e_3, e_4, e_5, e_6, e_7, e_8, e_9, e_{10}, e_{11}, e_{12}, e_{13}, e_{14}, e_{15}, e_{16}, e_{17}, e_{18}]$

where Ω_i^1 , $\Omega_i^{2,w}$ and (\bar{F}_i) are the collision operators responsible for viscous effects, surface tension effects, and fluid separation, respectively (Chen et al., 2019). The macroscopic variables are related to the distribution functions f_i^w via the following equations (Guo et al., 2002):

$$\rho^{w} = \sum f_{i}^{w} \tag{4}$$

$$\rho^{w} = \sum_{i} f_{i}^{w}$$

$$\rho^{w} \mathbf{u}^{w} = \sum_{i} f_{i}^{w} \mathbf{e}_{i} + \frac{\rho^{w} F}{2}$$

$$\rho = \sum_{w} \rho^{w}$$

$$\rho \mathbf{u} = \sum_{w} \rho^{w} \mathbf{u}^{w}$$

$$(5)$$

$$(6)$$

$$(7)$$

$$\rho = \sum_{w} \rho^{w} \tag{6}$$

$$\rho \mathbf{u} = \sum_{w}^{w} \rho^{w} \mathbf{u}^{w} \tag{7}$$

where ρ denotes the fluid density and \boldsymbol{u} denotes the fluid velocity. In the color-gradient models, the viscous collision operator Ω_i^1 is calculated collectively on the total distribution function (Lallemand and Luo, 2000), that is:

$$\Omega_i^1 = \mathbf{M}^{-1} \mathbf{S} \mathbf{M} (f_i - f_i^{eq}) \tag{8}$$

where M is a transformation matrix that transforms f_i into moment space, f_i^{eq} is the equilibrium distribution function, and S is a diagonal collision matrix defined as follows:

$$\mathbf{S} = \operatorname{diag}(0, s_e, s_{\xi}, 0, s_q, 0, s_q, 0, s_q, s_v, s_{\pi}, s_v, s_{\pi}, s_v, s_v, s_m, s_m, s_m)$$
(9)

where s_v is related to the fluid viscosity.

In order to achieve better stability and accuracy and reduce the spurious velocities at the interface (Chen et al., 2019), the lattice Boltzmann MRT (Lallemand and Luo, 2000; d'Humières et al., 2002) framework is employed. The lattice Boltzmann equation with the MRT collision operator can be expressed as (Yang and Wang, 2023):

$$f_{i}^{w}(x+e_{i}\delta t,t+\delta t) = f_{i}^{w}(x,t) + \Omega_{i}^{2,w} \left[-\mathbf{M}^{-1}\mathbf{S}(\mathbf{M}\mathbf{f}(x,t) - \mathbf{m}^{eq}) + \delta t\mathbf{M}^{-1} \left(\mathbf{I} - \frac{\mathbf{S}}{2} \right) \widehat{\mathbf{F}} \right]$$
(10)

where f denotes the vector form of the total distribution functions, and m^{eq} stands for the equilibrium moment. Additionally, $\hat{F} = M\bar{f}$ accounts for the forcing term in the moment space. For the D3Q19 lattice adopted by this work for 3D simulations, the equilibrium moments m^{eq} and the forcing moments \hat{F} can be calculated via the macroscopic variables directly:

$$\mathbf{m}^{eq} = \begin{bmatrix} \rho \\ -11\rho + 19\rho(u_x^2 + u_y^2 + u_z^2) \\ 3\rho - \frac{11}{2}\rho(u_x^2 + u_y^2 + u_z^2) \\ \rho u_x \\ -\frac{2}{3}u_x \\ \rho u_y \\ -\frac{2}{3}u_z \\ \rho u_z \\ -\frac{2}{3}u_z \\ \rho(2u_x^2 - u_y^2 - u_z^2) \\ -\frac{1}{2}\rho(2u_x^2 - u_y^2 - u_z^2) \\ \rho(u_y^2 - u_z^2) \\ -\frac{1}{2}\rho(u_y^2 - u_z^2) \\ \rho u_x u_y \\ \rho u_y u_z \\ \rho u_x u_z \\ 0 \\ 0 \\ 0 \end{bmatrix}$$

$$(11)$$

$$\begin{array}{c}
38\mathbf{u} \cdot \mathbf{F} \\
-11\mathbf{u} \cdot \mathbf{F} \\
F_{x} \\
-\frac{2}{3}F_{x} \\
F_{y} \\
-\frac{2}{3}F_{y} \\
F_{z} \\
-\frac{2}{3}F_{z} \\
2(2F_{x}u_{x} - F_{y}u_{y} - F_{z}u_{z}) \\
-(2F_{x}u_{x} - F_{y}u_{y} - F_{z}u_{z}) \\
2(F_{y}u_{y} - F_{z}u_{z}) \\
-(F_{y}u_{y} - F_{z}u_{z}) \\
F_{x}u_{x} + F_{y}u_{y} \\
F_{y}u_{y} + F_{z}u_{z} \\
0 \\
0 \\
0
\end{array}$$
(12)

0

where u_x , u_y , and u_z are the components of u in the x, y, and z directions, respectively.

In the color-gradient models, a body force F is introduced, that is responsible for surface tension:

$$\mathbf{F} = \frac{1}{2} \sigma \kappa \mathbf{C} \tag{13}$$

where σ denotes the surface tension, κ denotes the interfacial curvature, and \boldsymbol{C} is the color gradient defined via the isotropic gradient operator proposed by Leclaire et al. (2011):

$$\mathbf{C} = \nabla \phi = \frac{3}{\delta t} \sum_{i} \omega_{i} e_{i} \phi(t, x + e_{i} \delta t)$$
 (14)

where ω_i represents the weight coefficient in the D3Q19 model. The order parameter ϕ is defined as follows:

$$\phi = \frac{\rho_r - \rho_b}{\rho_r + \rho_b} \tag{15}$$

 $\phi = \frac{\rho_r - \rho_b}{\rho_r + \rho_b} \eqno(15)$ where ρ_b and ρ_r denote the densities of fluid b and fluid r, respectively.

The color function value $\phi = 1, -1, 0$ corresponds to pure "red" fluid, pure "blue" fluid, and the fluid-fluid interface, respectively. Using the color gradient \boldsymbol{C} , the interfacial curvature can be calculated as:

$$\kappa = [(\mathbf{I} - \mathbf{n}\mathbf{n}) \cdot \nabla] \cdot \mathbf{n} \tag{16}$$

where n denotes the normal direction of the color gradient C:

$$\mathbf{n} = \frac{|\nabla \phi|}{\nabla \phi} \tag{17}$$

Then, the contact angle θ between the three-phase contact line can be expressed as (Yang and Wang, 2023):

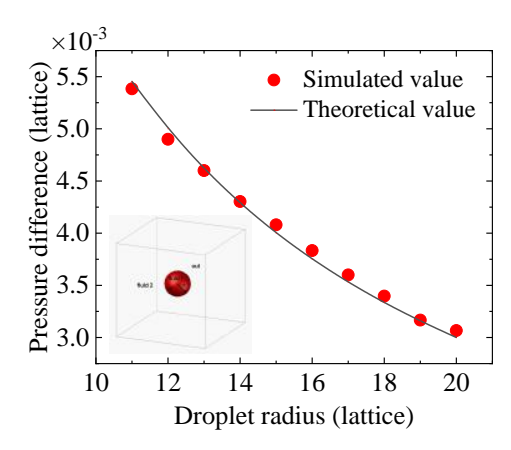


Fig. 1. Surface tension verification for numerical model.

$$\cos \theta = \frac{|\boldsymbol{e}_i \cdot \boldsymbol{C}|}{|\boldsymbol{e}_i||\boldsymbol{C}|} \tag{18}$$

2.2 Benchmark of multiphase flow

In order to verify the accuracy of the LBM algorithm described above, the following benchmark tests are conducted:

(1) Surface tension validation

This study employs the LBM to validate a multiphase flow system dominated by surface tension. Initially, a liquid droplet is placed within an $80 \times 80 \times 80$ hollow cubic domain. Under gravity-free conditions, the droplet stabilizes into a spherical shape suspended at the center of the cubic domain. By varying the droplet radius, the pressure difference between the interior and exterior of the droplet can be calculated.

According to the Laplace equation:

$$\Delta P = \frac{2\sigma}{r} \tag{19}$$

where ΔP denotes the pressure difference, r represents the droplet radius.

Initially, cubic droplets with edge lengths ranging from 10 to 20 lattice are simulated. All simulations are performed in lattice units (consistent throughout this study), with the interfacial tension coefficient $\sigma = 0.03$. As illustrated in Fig. 1, the simulation results exhibit excellent agreement with the Laplace equation.

(2) Wettability validation

The wettability of a solid surface can be characterized by measuring the static contact angle. Similar to the previous case, a liquid droplet is placed on the lower wall of an $80 \times 80 \times 80$ hollow cubic domain. Under gravity-free conditions, the droplet stabilizes into a hemispherical shape adhered to the wall. In this case, the relationship between preset contact angles in simulation configurations is investigated and the static contact angles are experimentally measured. Fig. 2 compares the simulated contact angles with predefined values, demonstrating that the geometric wettability boundary conditions accurately replicate two-phase wettability behavior.

(3) Capillary flow validation

This study further validates dynamic two-phase flow through capillary phenomena. Considering a two-phase flow in a cylindrical tube initially saturated with red-phase fluid, the inlet and outlet are connected to blue-phase and red-phase

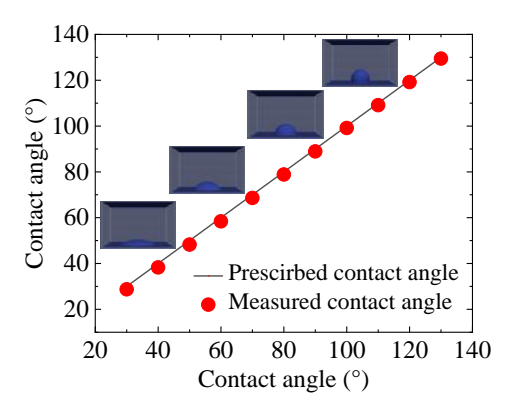


Fig. 2. Verification of different contact angles for LBM simulations.

reservoirs with constant pressures, respectively. Driven by the pressure difference ΔP and capillary forces, the red phase is displaced by the blue phase. In micro/nanoscale capillary flow, gravitational and inertial effects are negligible ($Re \ll 1$). The temporal evolution of the interface position can be derived as follows:

From Darcy's law:

$$Q = \frac{kA\Delta P}{\mu l} \tag{20}$$

where Q denotes the flow rate, which is equal to the product of v and A; v represents the velocity, defined as the distance traveled by the interface per unit time, i.e., dl/dt; k stands for permeability, and in a circular tube, its value is equal to the square of the radius (r^2) divided by 8.

Under spontaneous imbibition conditions, the interface displacement is dominated by capillary pressure P_c :

$$\Delta P = P_c = \frac{2\sigma}{r}\cos\theta\tag{21}$$

Combining the above equations yields:

$$\frac{\mathrm{d}l}{\mathrm{d}t} = \frac{r\sigma\cos\theta}{4[\mu_{nw}(L-l) + \mu_w l]} \tag{22}$$

where L denotes the tube length, while μ_{nw} and μ_{w} represent the dynamic viscosities of the non-wetting phase and the wetting phase, respectively.

Three scenarios are considered:

Case I: $\mu_{nw} = 0$, thus Eq. (22) is reduced to:

$$l = \sqrt{\frac{r\sigma\cos\theta}{2\mu_w}t + H} \tag{23}$$

which corresponds to the classical Lucas-Washburn equation, where σ denotes the surface tension and H is a constant.

Case II: $\mu_{nw} = \mu_w$, thus Eq. (22) is reduced to:

$$l = \frac{r\sigma\cos\theta}{4\mu L}t + H\tag{24}$$

Case III: $\mu_{nw} \neq \mu_w$, thus Eq. (22) is reduced to:

$$\frac{1}{2}Bl^2 + El - Gt - H = 0 (25)$$

where $B = 4(\mu_w - \mu_{nw})$, $E = 4\mu_{nw}L$, and $G = \sigma r \cos \theta$.

Simulations using LBM were validated against Eqs. (24) and (25). As shown in Fig. 3, the numerical results exhibited

excellent agreement with theoretical predictions across varying viscosity ratios.

3. Results and discussion

3.1 Properties of reconstructed porous structures

As previously described, this study employs the QSGS method to iteratively reconstruct the original 3D pore images. By modulating the number of initial random seed points, three 3D pore structures with comparable porosity but distinct pore size distributions were constructed, as shown in Figs. 4-5. These models are labeled sequentially as Low-permeability model, Moderate-permeability model, and High-permeability model from left to right.

On the basis of the LBM method, constant pressure boundaries were imposed at the inlet and outlet. Combined with Darcy's law, the permeability of three 3D pore structures with distinct pore size distributions was numerically calculated, and the structural parameters are summarized in Table 1.

3.2 Effect of rock permeability on multiphase flow

The intrinsic permeability of a porous medium is fundamentally governed by its pore architecture. The heterogeneity of structural permeability refers to spatial variations in permeability that arise from microscale differences in pore size, geometry and connectivity, which directly influences the pressure field, the balance between capillary and viscous forces, and the distribution of residual phases during fluid displacement, thereby altering both the displacement pathways and the overall efficiency. To investigate the effects of permeability heterogeneity on displacement efficiency, simulations were performed under a contact angle of $\theta=30^\circ$, with constant velocity boundary conditions applied at both the inlet and the outlet. Under identical displacement pressure conditions, the resulting multiphase distributions revealed marked variations across cores with differing intrinsic permeabilities (Fig. 6).

A preliminary comparative analysis indicated that highpermeability cores tend to exhibit well-connected pore networks and reduced tortuosity, which promote the formation of preferential flow channels under pressure gradients and leads to relatively uniform velocity distributions and higher average flow velocities. In contrast, low-permeability cores are characterized by more complex pore architectures that impose greater tortuosity on flow paths, thereby intensifying capillary resistance and viscous dissipation. These effects manifest as spatially heterogeneous velocity fields, including localized regions of flow stagnation. To systematically validate the scientific rigor of these initial observations, this study introduces the use of fractal dimension (D) and Euler number (χ) as quantitative descriptors of the connectivity patterns formed by the invading fluid phase during displacement. It is important to emphasize that these metrics are not adopted to characterize the inherent structural complexity or topology of the porous medium itself but rather to quantify the dynamic evolution of fluid-phase connectivity throughout the seepage

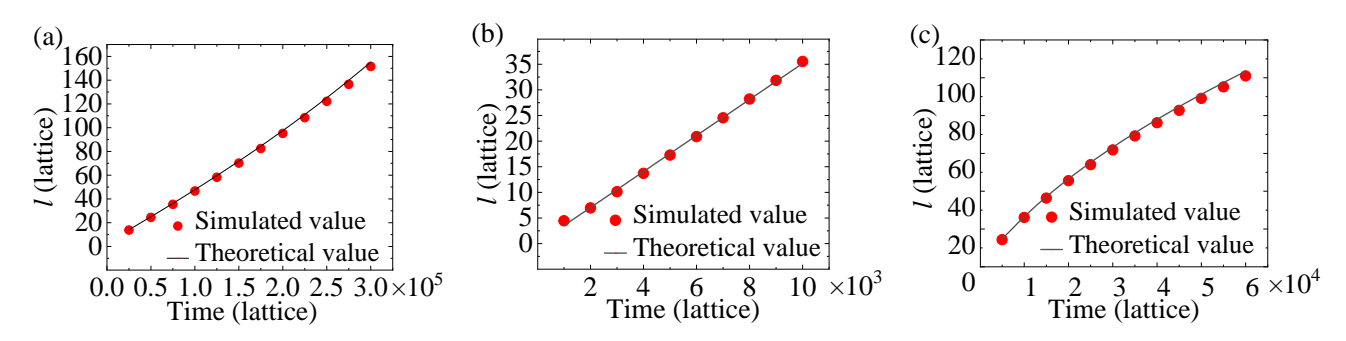


Fig. 3. Comparison of interfacial position variation between LBM simulation and theoretical values for spontaneous imbibition in a capillary tube, with a contact angle of 30° and viscosity ratio μ_{nw}/μ_w of (a) 0.1, (b) 1 and (c) 10.

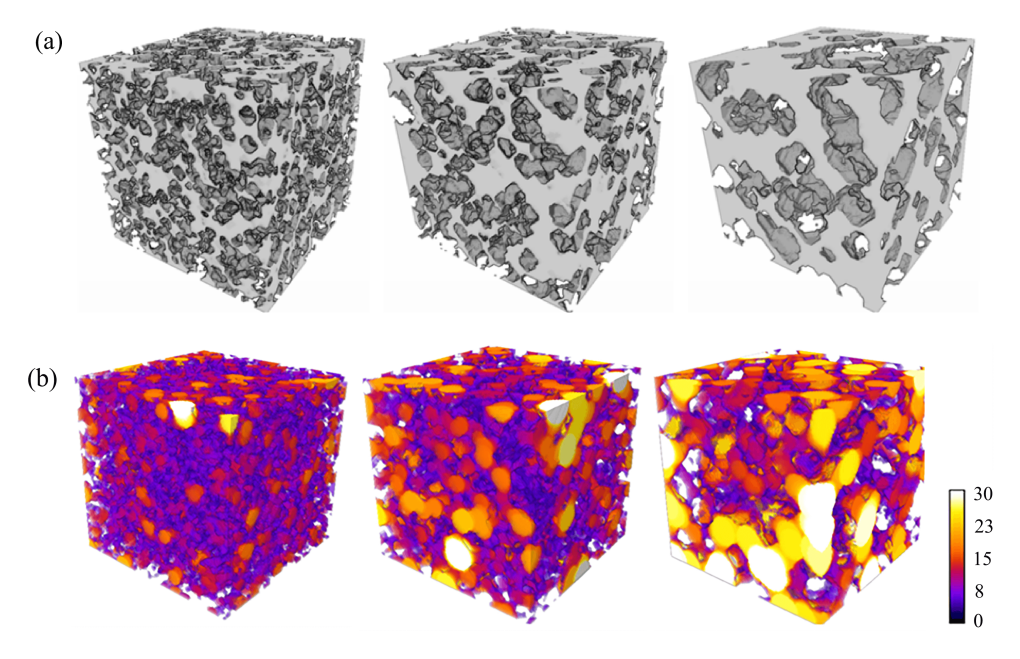


Fig. 4. (a) Binary structures of the three core samples and (b) 3D pore size distribution of the three core samples. (The gray part in (a) represents the pore space in porous media and the solid part is transparent. The colorbar in (b) shows that the variations in pore size are indicated by the colors: White represents large pores and black represents small pores.).

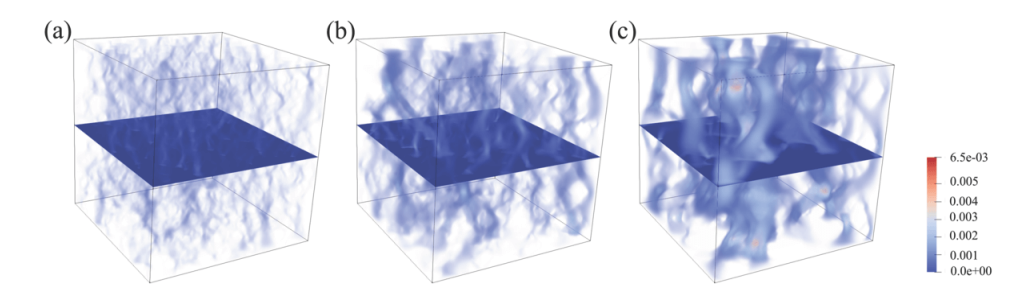


Fig. 5. Flow field heterogeneity in porous media with different permeabilities: (a) Low-permeability model, (b) moderate-permeability model and (c) high-permeability model. (The colorbar indicates the fluid velocity.).

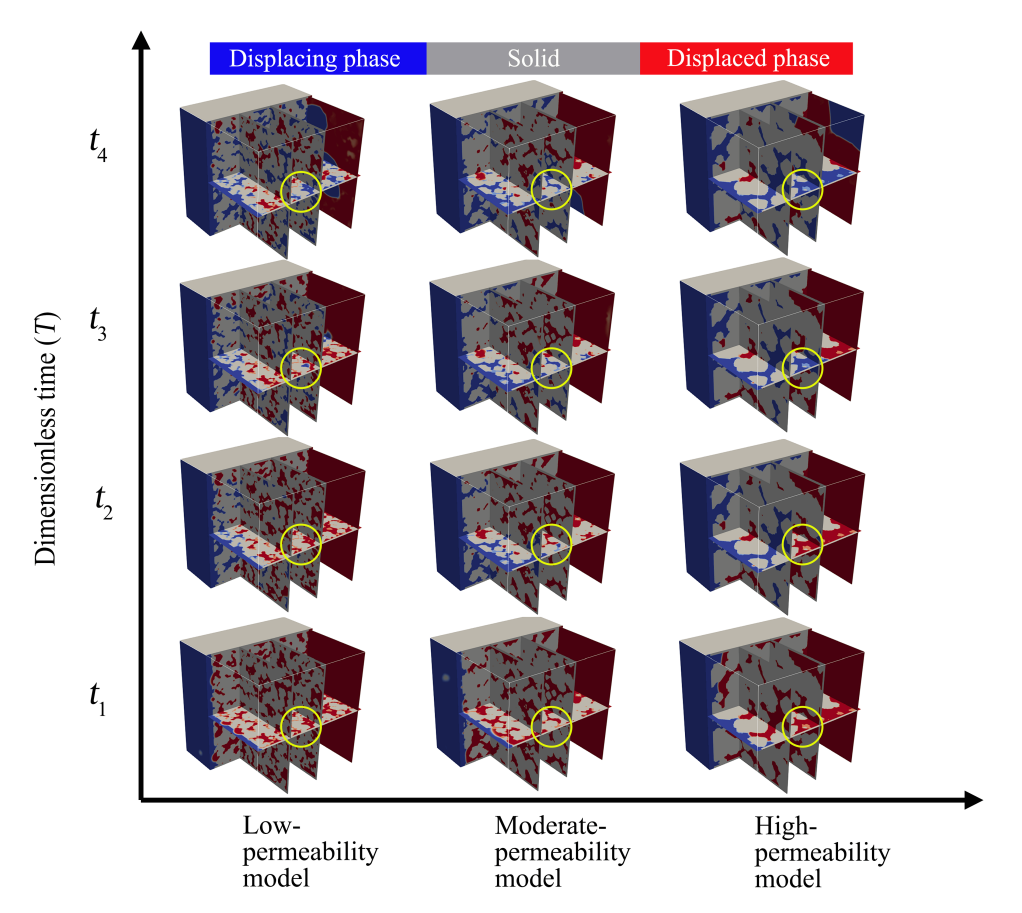


Fig. 6. Evolution of immiscible fluid displacement in porous media with different permeabilities and contact angle of 30°. The horizontal axis denotes the porous structure with different permeabilities, and the vertical axis represents dimensionless time stages, with t_1 - t_4 corresponding to normalized times 0, 1/3, 2/3, and 1, respectively. Yellow circles highlight representative two-phase fluid distributions at each time step, illustrating the effects of wettability on displacement patterns.

Table 1. Parameters of three core models.

| Model | Grid count (lattice ³) | Porosity (%) | Mean pore size (μm) | Permeability (mD) |
|-----------------------|------------------------------------|--------------|---------------------|-------------------|
| Low-permeability | $266\times266\times256$ | 27.26 | 30.92 | 359 |
| Moderate-permeability | $266\times266\times256$ | 28.03 | 45.56 | 807 |
| High-permeability | $266\times266\times256$ | 27.97 | 69.69 | 2,801 |

process.

The fractal dimension (D) quantifies the spatial complexity of pore systems (Dathe et al., 2001; Li and Huang, 2015; Fu et al., 2017), reflecting surface roughness and structural heterogeneity:

$$D = \frac{\log N}{\log \frac{1}{\varepsilon}}$$
 where N represents the number of pores and ε denotes pore

size.

The Euler number (χ) (Ziou and Allili, 2002; Ozden, 2010; Qin et al., 2022) characterizes the topological connectivity of 3D pore structures:

$$\chi = \beta_0 - \beta_1 + \beta_2 \tag{27}$$

where β_0 stands for number of isolated objects (connected components), β_1 denotes redundant connections (pore throats), and β_2 denotes enclosed cavities (voids within pores).

To characterize the spatial distribution of the injection fluid flow paths, as shown in Fig. 7, the temporal evolution of the Euler number was analyzed on the basis of quantifying the fluid topology during multiphase flow. The results showed that increasing permeability markedly reduces the negative value of Euler numbers, indicating the enhanced continuity of fluid-phase networks in high-permeability media and a corresponding reduction in topological complexity. This observation suggests that higher permeability improves the topological connectivity of the fluid distribution, as evidenced by fewer isolated pore clusters and the dominance of continuous primary flow pathways.

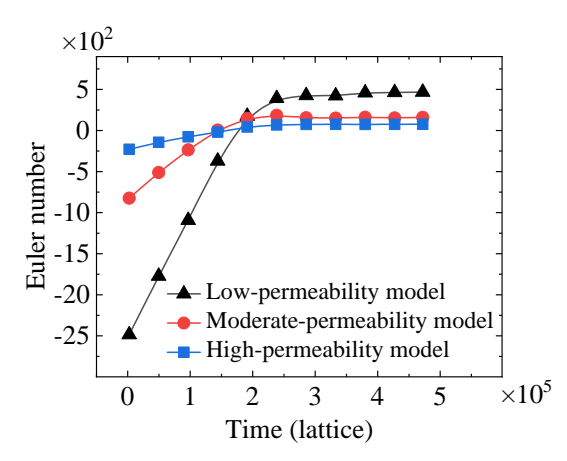


Fig. 7. Temporary variation in injecting fluid topology in porous media with different permeabilities.

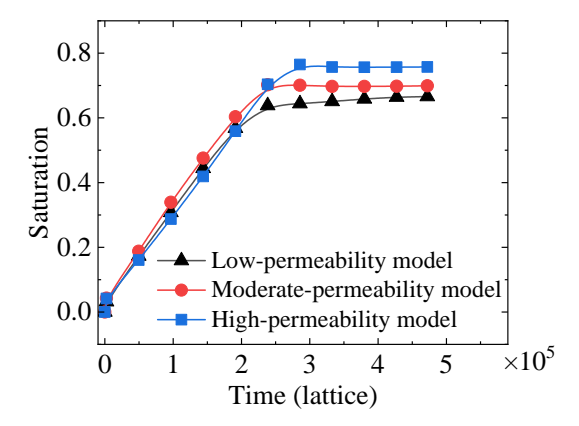


Fig. 8. Temporal evolution patterns of displacing phase saturation in porous media with different permeabilities.

Building upon systematic analyses of the temporal evolution of fluid saturation (Fig. 8) and variations in breakthroughphase saturation across different cores (Table 2), this study establishes a quantitative relationship between core permeability and displacement efficiency. The numerical results reveal a strong positive correlation, which is attributed to permeability-governed displacement mechanisms dictated by pore architecture. High-permeability cores, characterized by large-aperture pore networks (mean pore size = $69.69 \mu m$), exhibit displacement efficiencies in the range of 70% to 80%. These structures support stable frontal advancement and suppress viscous fingering instabilities, thereby enhancing overall efficiency. In contrast, low-permeability cores with smaller pore sizes (mean = 30.92 µm) exhibit significantly lower displacement efficiencies (40% to 50%). The dense and tortuous networks in these systems amplify capillary forces and promote non-wetting phase entrapment.

As illustrated in Fig. 9, the heterogeneity of structural permeability plays a critical role in governing the spatial distribution of displacement pathways. This divergence originates from the heterogeneous distribution of flow resistance within the medium. According to Darcy's law, local seepage velocity is positively correlated with local permeability, facilitating the formation of low-resistance preferential channels in regions with high permeability – typically associated with large pores

Table 2. Saturation and breakthrough time for the three core samples.

| Model | Saturation | Breakthrough time (lattice) |
|-----------------------|------------|-----------------------------|
| Low-permeability | 0.59529 | 129,800 |
| Moderate-permeability | 0.66785 | 96,400 |
| High-permeability | 0.75087 | 84,210 |

or highly connected networks. During displacement, fluids preferentially migrate through these paths, significantly reducing the breakthrough time of the displacing phase (Table 2). From an energetic standpoint, this behavior aligns with the principle of minimized energy dissipation in porous systems: The fluid optimizes flow paths by selecting regions of least hydraulic resistance, thereby achieving an energetically favorable distribution of flow potential.

Overall, the integrated analysis of quantitative data and phase connectivity diagrams underscores the central role of porous media heterogeneity in controlling displacement efficiency. In high-permeability systems, enhanced efficiency is achieved through low-tortuosity, high-conductivity flow pathways; conversely, in low-permeability media, efficiency declines due to capillary trapping effects associated with microscale pores and poorly connected pathways.

3.3 Effect of wettability on multiphase flow

Wettability, as a governing factor in fluid migration through porous media, governs displacement behavior by regulating the dynamic equilibrium between capillary and viscous forces (Nhunduru et al., 2022). This section presents the simulation results from the moderate-permeability core model (Fig. 10). All cases share a constant capillary number ($Ca = 9.16 \times 10^{-6}$) and surface tension ($\sigma = 0.0881$), isolating the wettability effect by varying the contact angle (30° , 70° , 110° and 150°). The analysis examines the temporal evolution of fluid saturation (Fig. 11) and the resulting breakthrough-phase saturation distributions (Fig. 12).

The results demonstrate that wettability exerts a decisive influence on microscopic phase distribution during displacement. Strongly-wetting phases preferentially invade smaller pores, forming continuous flow pathways, whereas weakly-wetting phases are increasingly prone to entrapment due to capillary resistance. Variations in contact angle significantly modulate the behavior of the three-phase contact line. When the contact angle is below 90°, capillary forces enhance the advancement of the displacement front. However, at contact angles above 90°, increased capillary resistance impedes the progression of the displacing phase, thereby reducing displacement efficiency. These findings are consistent with classical theories of capillary-dominated displacement (Chen et al., 2023).

In order to further elucidate the wettability-governed flow mechanisms, the dynamic evolution of pore-scale topological parameters was analyzed during immiscible displacement in the moderate-permeability model. A contact-angle-controlled

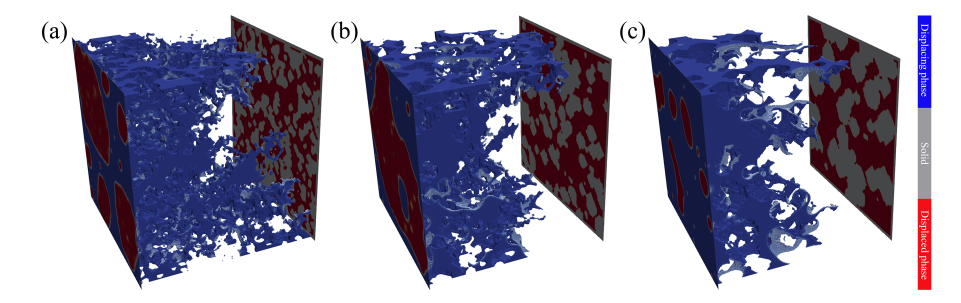


Fig. 9. Displacement path topological configurations in porous media with different permeabilities: (a) Low-permeability model, (b) moderate-permeability model and (c) high-permeability model. (The blue and red parts represent the invading and defending fluids, respectively).

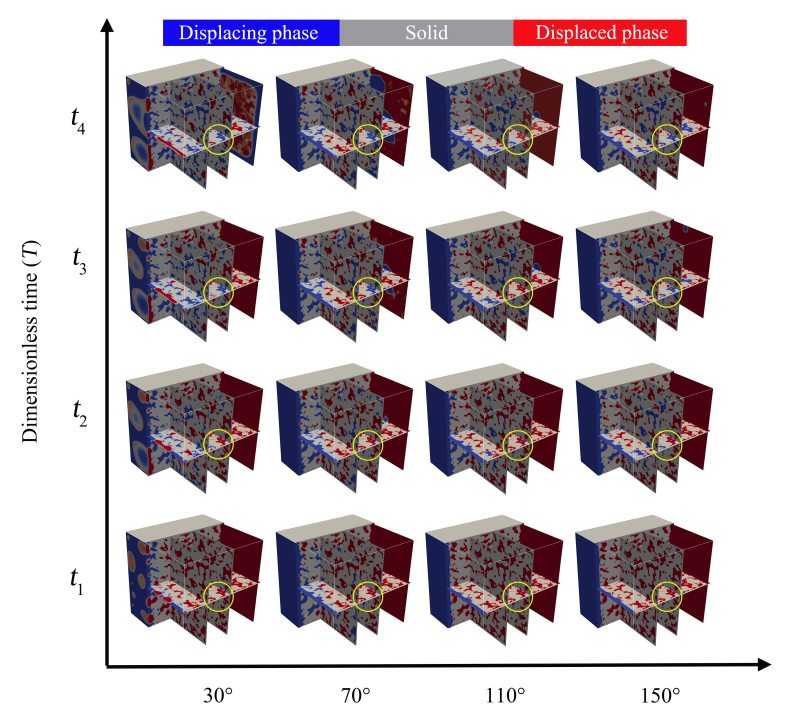


Fig. 10. Evolution of immiscible fluid displacement in a moderate-permeability core under different contact angle conditions. The horizontal axis denotes the contact angle and the vertical axis represents dimensionless time stages, with t_1 - t_4 corresponding to normalized times 0, 1/3, 2/3, and 1, respectively. The yellow circles highlight representative two-phase fluid distributions at each time step, illustrating the effects of wettability on displacement patterns.

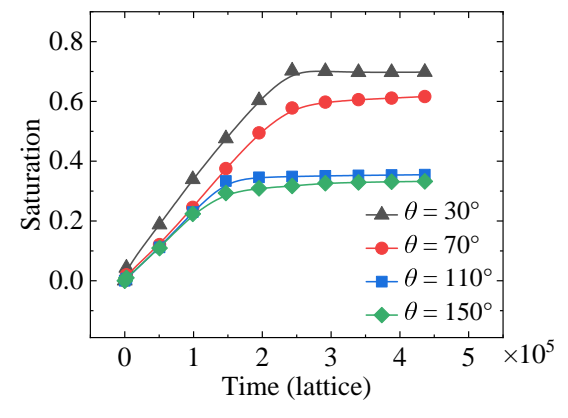


Fig. 11. Temporal evolution of invading phase saturation in porous media with different contact angles.

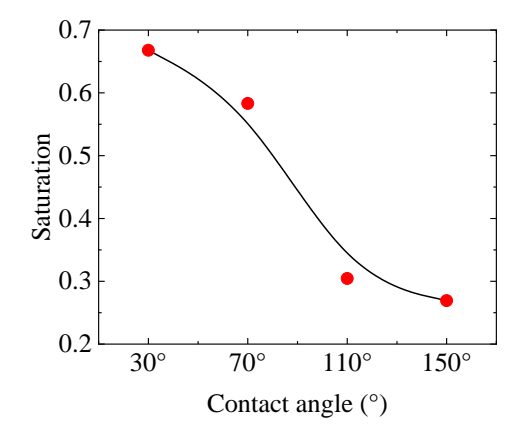


Fig. 12. Effect of contact angle on injecting fluid saturation at breakthrough state.

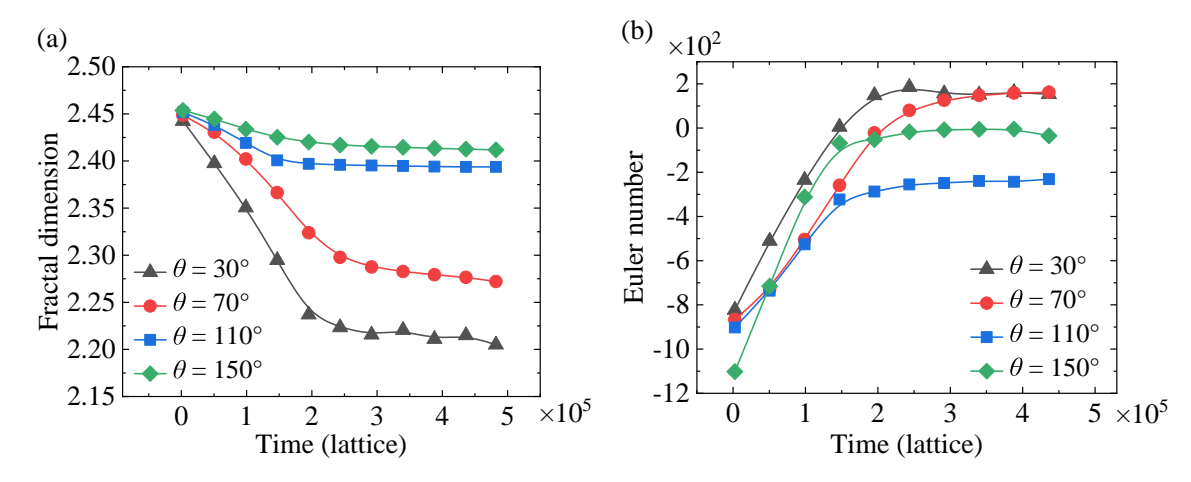


Fig. 13. Temporary variation in immiscible displacement interface in porous media: (a) Fractal dimension and (b) Euler number.

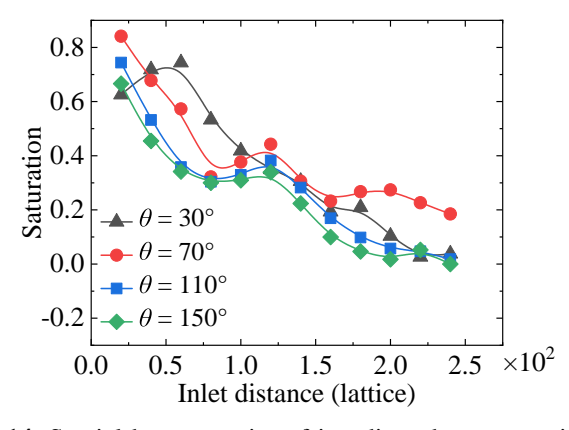


Fig. 14. Spatial heterogeneity of invading phase saturation at breakthrough state during multiphase flowtle.

LBM multiphase flow model ($\theta = 30^{\circ}-150^{\circ}$) was coupled with multiscale topological descriptors – namely, fractal dimension (D) and Euler number (χ) – to quantify the effect of wettability on displacement behavior.

The simulation results (Fig. 13) revealed that increasing the contact angle, which corresponds to more hydrophobic conditions, significantly alters capillary-driven selective invasion. As the capillary resistance intensifies, the displacing fluid is increasingly restricted from entering smaller pores, but instead is redirected through larger, more conductive pathways. Consequently, the structural modifications become localized within large-scale pore networks. This behavior suppresses branching flow through fine-scale structures, reflected by reduced fluctuations in the fractal dimension during displacement. Concurrently, hydrophobic conditions lead to residual phase entrapment in the form of connected clusters within larger pores, thereby minimizing the formation of isolated cavities, as indicated by a less negative Euler number. The enhanced connectivity between large pores further diminishes topological isolation. The combined evolution of D and γ clearly demonstrates that wettability governs pore-scale displacement dynamics by limiting small-pore participation and favoring large pore-dominated flow pathways.

The above insights carry important implications for the

optimization of immiscible displacement efficiency and the prediction of fluid transport behavior in porous media. A comparative analysis of cross-sectional saturation distributions at breakthrough under various contact angles (Fig. 14) also supports these conclusions.

Overall, the systematic data presented in this section confirm that wettability variations in porous media fundamentally modulate displacement patterns by redistributing capillary forces. Under hydrophilic conditions, the invading fluid preferentially follows thermodynamically favorable pore pathways, enhancing displacement continuity and efficiency.

3.4 Mutual effects of wettability and permeability

During immiscible displacement in heterogeneous porous media, the interplay between permeability and wettability is a critical factor that governs the evolution of fluid-phase topology. High-permeability cores, characterized by enhanced pore connectivity and larger throat apertures, promote the development of continuous, low-complexity backbone drainage networks for the non-wetting phase. This is evidenced by the most negative values of the Euler characteristic and the lowest observed fractal dimensions. In contrast, low-permeability cores, limited by narrower pore throats, cause increased flow path fragmentation and branching events, resulting in more negative Euler characteristics and elevated fractal dimensions.

Wettability influences interfacial stability through capillary forces, as described by $(P_c = (2\sigma\cos\theta)/r)$. An increase in contact angle (from 30° to 150°) significantly amplifies capillary fingering, causing the non-wetting phase to preferentially invade larger throats. This behavior gives rise to highly branched, dendritic displacement structures, reflected in simultaneous increases in both the negative Euler characteristic and the fractal dimension as the contact angle increases. The coupled effects of permeability and wettability reveal a distinct displacement behavior: Systems with high permeability and low contact angles promote stable displacement fronts through enhanced capillary stabilization, yielding efficiently connected fluid pathways with minimal topological complexity. Con-

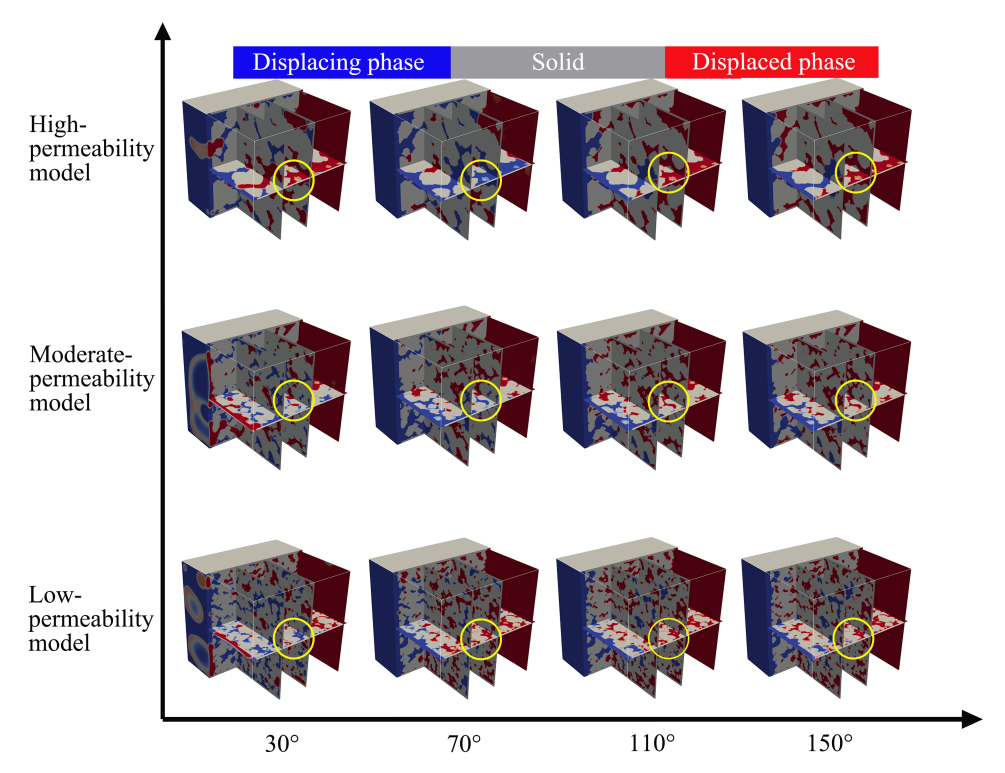


Fig. 15. Immiscible displacement pattern in porous media at breakthrough state under different contact angles and permeability.

versely, combinations of low permeability and high contact angles intensify capillary fingering and promote the formation of multiscale, branched architectures, which increase tortuosity and enhance wetting-phase entrapment – the hallmarks of high topological complexity.

The above interactions collectively govern the non-equilibrium dynamics of multiphase flow in porous media, with supporting visualizations provided in Fig. 15. Fig. 16 depicts the coupling among contact angle, permeability, and displacement efficiency. It can be seen that merely increasing permeability does not significantly enhance displacement efficiency. Moreover, our results reveal a critical synergy between permeability and wettability (Fig. 18), manifested as a distinct non-monotonic relationship between contact angle and breakthrough efficiency in low-permeability media. This coupling effect controls the resulting fluid-phase morphology: With increasing contact angle, the fractal dimension of the displacing fluid also increases (Fig. 17), indicating more complex and branched invasion patterns under hydrophobic conditions.

This discrepancy stems from the inherent pore-structure heterogeneity and the dominant influence of capillary forces, which diminish the direct linear impact of permeability on flow behavior. Concurrently, larger contact angles (i.e., increased hydrophobicity) markedly reduce the displacement efficiency. Mechanistically, in hydrophilic media, the displacing phase (e.g., water) readily wets pore surfaces, leading to efficient displacement and low residual saturation of the defending phase (e.g., oil) at breakthrough. In contrast, under hydrophobic conditions, the invasion of the displacing phase is inhibited, promoting higher retention of the displaced phase and elevated

residual saturation of the displaced fluid upon breakthrough.

4. Conclusions

This study utilizes an integrated QSGS algorithm to efficiently generate 3D pore-scale models with permeability variations, overcoming the limitations of conventional methods and significantly reducing model construction time. The lattice Boltzmann method is applied to simulate multiphase displacement under various permeability and contact angle conditions, thus elucidating the coupling mechanism between pore structure and wettability. It is found that in low-permeability cores, the relationship between contact angle and permeability is nonmonotonic, while in medium- and high-permeability cores, displacement efficiency increases with increasing contact angle. The interaction between pore structure and wettability governs nonlinear flow behavior in porous media, disrupting the conventional assumption of a linear flow-efficiency relationship. Especially in low-permeability media, increased permeability does not consistently improve displacement efficiency.

The study emphasizes that evaluating displacement efficiency in heterogeneous porous systems requires a comprehensive consideration of topological connectivity, wettability-driven interfacial dynamics, and capillary constraints. However, the permeability-wettability-efficiency relationship established by the current model has limited generalizability, and the critical thresholds for maximizing displacement efficiency remain undetermined. Future studies should expand parameter ranges and incorporate machine learning-assisted sensitivity analysis to better quantify the complex relationship between microstructure and macroscopic flow behavior, thereby prov-

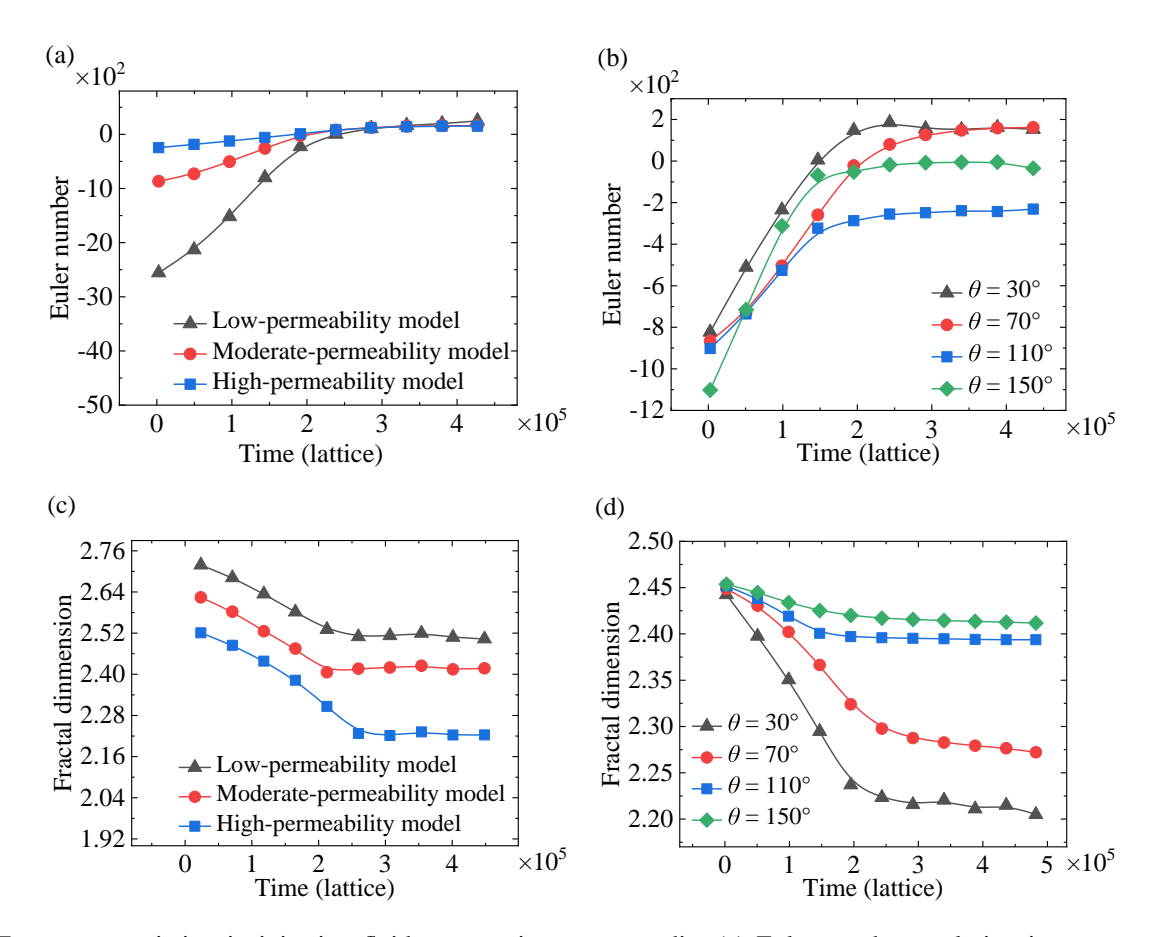


Fig. 16. Temporary variation in injecting fluid patterns in porous media: (a) Euler number evolution in porous media with different permeabilities, (b) Euler number evolution under different contact angles, (c) fractal dimension evolution in porous media with different permeabilities and (d) fractal dimension evolution under different contact angles.

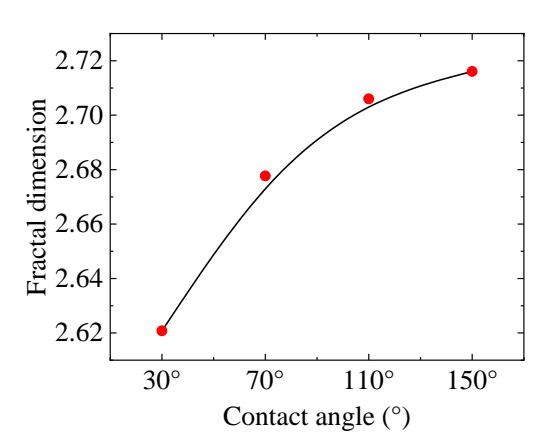


Fig. 17. Correlation between the contact angle and the fractal dimension of the displacing fluid at breakthrough in a low-permeability model.

iding a more reliable theoretical foundation for predicting multiphase flow in realistic geological media.

Acknowledgements

This work was financially supported by the Key R&D Program of Shandong Province, China (No. 2022CXGC020406), the NSF grant of China (No. 52404049) and the Science Foundation of China University of Petroleum, Beijing (No.

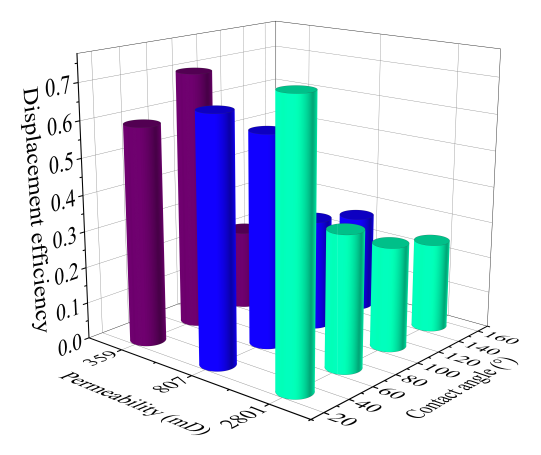


Fig. 18. Effect of contact angle and permeability on displacement efficiency in 3D porous media.

2462024SZBH004).

Additional information: Author's email

lijunchao@xsyu.edu.cn (J. Li)

Conflict of interest

The authors declare no competing interest.

Open Access This article is distributed under the terms and conditions of the Creative Commons Attribution (CC BY-NC-ND) license, which permits unrestricted use, distribution, and reproduction in any medium, provided the original work is properly cited.

References

- Bocanegra, J. A., Misale, M., Borelli, D. A systematic literature review on Lattice Boltzmann Method applied to acoustics. Engineering Analysis with Boundary Elements, 2024, 158: 405-429.
- Cai, J., Qin, X., Xia, X., et al. Numerical modeling of multiphase flow in porous media considering micro- and nanoscale effects: A comprehensive review. Gas Science and Engineering, 2024, 131, 205441.
- Chen, K., Liu, P., Wang, W., et al. Effects of capillary and viscous forces on two-phase fluid displacement in the microfluidic model. Energy & Fuels, 2023, 37(22): 17263-17276.
- Chen, Y., Valocchi, A. J., Kang, Q., et al. Inertial effects during the process of supercritical CO₂ displacing brine in a sandstone: Lattice Boltzmann simulations based on the continuum-surface-force and geometrical wetting models. Water Resources Research, 2019, 55(12): 11144-11165.
- Cieplak, M., Robbins, M. O. Dynamical transition in quasistatic fluid invasion in porous media. Physical Review Letters, 1988, 60(20): 2042-2045.
- d'Humières, D., Ginzburg, I., Krafczyk, M., et al. Multiplerelaxation-time lattice Boltzmann models in three dimensions. Philosophical Transactions of the Royal Society of London Series A: Mathematical, Physical and Engineering Sciences, 2002, 360(1792): 437-451.
- Dathe, A., Eins, S., Niemeyer, J., et al. The surface fractal dimension of the soil-pore interface as measured by image analysis. Geoderma, 2001, 103(1-2): 203-229.
- Deng, H., Bielicki, J. M., Oppenheimer, M., et al. Leakage risks of geologic CO₂ storage and the impacts on the global energy system and climate change mitigation. Climatic Change, 2017, 144(2): 151-163.
- Fu, H., Tang, D., Xu, T., et al. Characteristics of pore structure and fractal dimension of low-rank coal: A case study of Lower Jurassic Xishanyao coal in the southern Junggar Basin, NW China. Fuel, 2017, 193: 254-264.
- Guo, Z., Zheng, C., Shi, B. Discrete lattice effects on the forcing term in the lattice Boltzmann method. Physical Review E, 2002, 65: 046308.
- Heinemann, N., Alcalde, J., Miocic, J. M., et al. Enabling large-scale hydrogen storage in porous media the scientific challenges. Energy & Environmental Science, 2021, 14(2): 853-864.
- Holtzman, R. Effects of pore-scale disorder on fluid displacement in partially-wettable porous media. Scientific Reports, 2016, 6: 36221.
- Holtzman, R., Segre, E. Wettability stabilizes fluid invasion into porous media via nonlocal, cooperative pore filling. Physical Review Letters, 2015, 115: 164501.
- Hu, R., Lan, T., Wei, G., et al. Phase diagram of quasi-static immiscible displacement in disordered porous media. Journal of Fluid Mechanics, 2019, 875: 448-475.

- Huang, H., Huang, J., Lu, X., et al. On simulations of highdensity ratio flows using color-gradient multiphase Lattice Boltzmann models. International Journal of Modern Physics C, 2013, 24(4): 1350021.
- Jackson, S. J., Lin, Q., Krevor, S. Representative elementary volumes, hysteresis, and heterogeneity in multiphase flow from the pore to continuum scale. Water Resources Research, 2020, 56: e2019WR026396.
- Jiang, Z., van Dijke, M. I. J., Sorbie, K. S., et al. Representation of multiscale heterogeneity via multiscale pore networks. Water Resources Research, 2013, 49(9): 5437-5449.
- Ju, Y., Gong, W., Chang, W., et al. Effects of pore characteristics on water-oil two-phase displacement in non-homogeneous pore structures: A pore-scale lattice Boltzmann model considering various fluid density ratios. International Journal of Engineering Science, 2020, 154: 103343.
- Ju, Y., Gong, W., Zheng, J. Effects of pore topology on immiscible fluid displacement: Pore-scale lattice Boltzmann modelling and experiments using transparent 3D printed models. International Journal of Multiphase Flow, 2022, 152: 104085.
- Jung, M., Brinkmann, M., Seemann, R., et al. Wettability controls slow immiscible displacement through local interfacial instabilities. Physical Review Fluids, 2016, 1: 074202.
- Lallemand, P., Luo, L. S. Theory of the lattice Boltzmann method: Dispersion, dissipation, isotropy, Galilean invariance, and stability. Physical Review E, 2000, 61(6): 6546-6562.
- Leclaire, S., Pellerin, N., Reggio, M., et al. Enhanced equilibrium distribution functions for simulating immiscible multiphase flows with variable density ratios in a class of lattice Boltzmann models. International Journal of Multiphase Flow, 2013, 57: 159-168.
- Leclaire, S., Pellerin, N., Reggio, M., et al. A multiphase lattice Boltzmann method for simulating immiscible liquid-liquid interface dynamics. Applied Mathematical Modelling, 2016, 40: 6376-6394.
- Leclaire, S., Pellerin, N., Reggio, M., et al. Unsteady immiscible multiphase flow validation of a multiple-relaxation-time lattice Boltzmann method. Journal of Physics A: Mathematical and Theoretical, 2014, 47: 105501.
- Leclaire, S., Reggio, M., Trepanier, J. Y. Isotropic color gradient for simulating very high-density ratios with a two-phase flow lattice Boltzmann model. Computers & Fluids, 2011, 48(1): 98-112.
- Lei, W., Gong, W., Wang, M. Wettability effect on displacement in disordered media under preferential flow conditions. Journal of Fluid Mechanics, 2023, 975: A33.
- Lei, W., Liu, T., Xie, C., et al. Enhanced oil recovery mechanism and recovery performance of micro-gel particle suspensions by microfluidic experiments. Energy Science & Engineering, 2020, 8(4): 986-998.
- Lei, W., Lu, X., Liu, F., et al. Non-monotonic wettability effects on displacement in heterogeneous porous media. Journal of Fluid Mechanics, 2022, 942: R5.

- Li, J., Liu, Y., Gao, Y., et al. Effects of microscopic pore structure heterogeneity on the distribution and morphology of remaining oil. Petroleum Exploration and Development, 2018, 45(6): 1112-1122.
- Li, T., Li, M., Jing, X., et al. Influence mechanism of porescale anisotropy and pore distribution heterogeneity on permeability of porous media. Petroleum Exploration and Development, 2019, 46(3): 594-604.
- Li, Y., Huang, R. Relationship between joint roughness coefficient and fractal dimension of rock fracture surfaces. International Journal of Rock Mechanics and Mining Sciences, 2015, 75: 15-22.
- Li, Y., Liu, H., Peng, C., et al. Insight into evolution of invasive patterns on fingering phenomenon during immiscible two-phase flow through pore structure. Petroleum Science, 2024, 21(5): 3307-3325.
- Massarweh, O., Abushaikha, A. S. CO₂ sequestration in subsurface geological formations: A review of trapping mechanisms and monitoring techniques. Earth-Science Reviews, 2024, 253: 104793.
- Nhunduru, R. A. E., Jahanbakhsh, A., Shahrokhi, O., et al. The impact of wettability on dynamic fluid connectivity and flow transport kinetics in porous media. Water Resources Research, 2022, 58: e2021WR030729.
- Ozden, H. Unification of generating function of the Bernoulli, Euler and Genocchi numbers and polynomials. AIP Conference Proceedings, 2010, 1281: 1125-1128.
- Peng, S., Tang, Z., Lei, B., et al. Design and application of bionic surface for directional liquid transportation. Progress in Chemistry, 2022, 34(6): 1321-1336.
- Prasad, S. K., Sangwai, J. S., Byun, H. S. A review of the supercritical CO₂ fluid applications for improved oil and gas production and associated carbon storage. Journal of CO₂ Utilization, 2023, 72: 102479.
- Qin, X., Xia, Y., Wu, J., et al. Influence of pore morphology on permeability through digital rock modeling: New insights from the Euler number and shape factor. Energy & Fuels, 2022, 36(14): 7519-7530.
- Shan, X., Chen, H. Lattice Boltzmann model for simulating flows with multiple phases and components. Physical Review E, 1993, 47(3): 1815.
- Singh, K., Scholl, H., Brinkmann, M., et al. The role of local instabilities in fluid invasion into permeable media. Scientific Reports, 2017, 7: 444.
- Swift, M. R., Osborn, W. R., Yeomans, J. M. Lattice Boltzmann simulation of nonideal fluids. Physical Review Letters, 1995, 75(5): 830-833.
- Wang, M., Pan, N., Wang, J., et al. Mesoscopic simulations

- of phase distribution effects on the effective thermal conductivity of microgranular porous media. Journal of Colloid and Interface Science, 2007a, 311(2): 562-570.
- Wang, M., Wang, J., Pan, N., et al. Mesoscopic predictions of the effective thermal conductivity for microscale random porous media. Physical Review E, 2007b, 75: 036702.
- Wang, S. Reveal the secret of super-wetting and slippery on the peristome surface of nepenthes alata: Jiang-Taylor capillary rise and directional liquid transport. Progress in Chemistry, 2017, 29(1): 3-4.
- Wei, C., Yan, J., Tang, H., et al. Fabrication and application of slippery liquid-infused porous surface. Progress in Chemistry, 2016, 28(1): 9-17.
- Wu, D., Hu, R., Lan, T., et al. Role of pore-scale disorder in fluid displacement: Experiments and theoretical model. Water Resources Research, 2021, 57: e2020WR028004.
- Yang, C., Li, H., Fang, Y., et al. Effects of groundwater pumping on ground surface temperature: A regional modeling study in the North China plain. Journal of Geophysical Research: Atmospheres, 2020, 125: e2019JD031764.
- Yang, G., Wang, M. Surface roughness effect on dynamic wettability in imbibition process. Computers & Fluids, 2023, 263: 105959.
- Yang, X., Hu, J., Ma, R., et al. Integrated hydrologic modelling of groundwater-surface water interactions in cold regions. Frontiers in Earth Science, 2021, 9: 721009.
- Yang, Y., Wang, S., Chen, L., et al. Shale oil flow mechanisms during fracturing-soaking-producing process studied by Lattice Boltzmann simulation. Petroleum Science Bulletin, 2025, 10(2): 298-308. (in Chinese)
- Zhang, L., Wang, M. Modeling of electrokinetic reactive transport in micropore using a coupled lattice Boltzmann method. Journal of Geophysical Research: Solid Earth, 2015, 120(5): 2877-2890.
- Zhan, X., Jin, B., Zhang, Q., et al. Design and applications of multifunctional super-wetting materials. Progress in Chemistry, 2018, 30(1): 87-100.
- Zheng, J., Lei, W., Ju, Y., et al. Investigation of spontaneous imbibition behavior in a 3D pore space under reservoir condition by lattice Boltzmann method. Journal of Geophysical Research: Solid Earth, 2021, 126: e2021JB021987.
- Zhou, Y., Guan, W., Zhao, C., et al. Numerical methods to simulate spontaneous imbibition in microscopic pore structures: A review. Capillarity, 2024, 11(1): 1-21.
- Ziou, D., Allili, M. Generating cubical complexes from image data and computation of the Euler number. Pattern Recognition, 2002, 35(12): 2833-2839.